ACS APPLIED MATERIALS & INTERFACES

Research Article

www.acsami.org

SnO_2 Nanoslab as NO_2 Sensor: Identification of the NO_2 Sensing Mechanism on a SnO_2 Surface

Sunglyul Maeng,*[,†] Sang-Woo Kim,*[,‡] Deuk-Hee Lee,[§] Seung-Eon Moon,[∥] Ki-Chul Kim,[⊥] and Amitesh Maiti*[,#]

[†]Department of Electrical & Electronic Engineering, Woosuk University, Samrye-Eup, Wanju-Gun, Jeonbuk, 565-701, Republic of Korea

[‡]School of Advanced Materials Science and Engineering, SKKU Advanced Institute of Nanotechnology (SAINT), Center for Human Interface Nanotechnology (HINT), Sungkyunkwan University, Suwon 440-746, Republic of Korea

[§]Department of Electrical Engineering and Institute for Nano Science, Korea University, Seoul 136-701, Republic of Korea

[∥]IT Convergence Technology Research Laboratory, Electronics and Telecommunications Research Institute, 161 Gajeong-dong, Yuseong, Daejeon, 305-700, Republic of Korea

[⊥]Department of Advanced Chemical Engineering, Mokwon University, 800 Doan-dong, Seo-gu, Daejeon, 302-729, Republic of Korea

[#]Lawrence Livermore National Laboratory, Livermore, California 94551, United States

Supporting Information

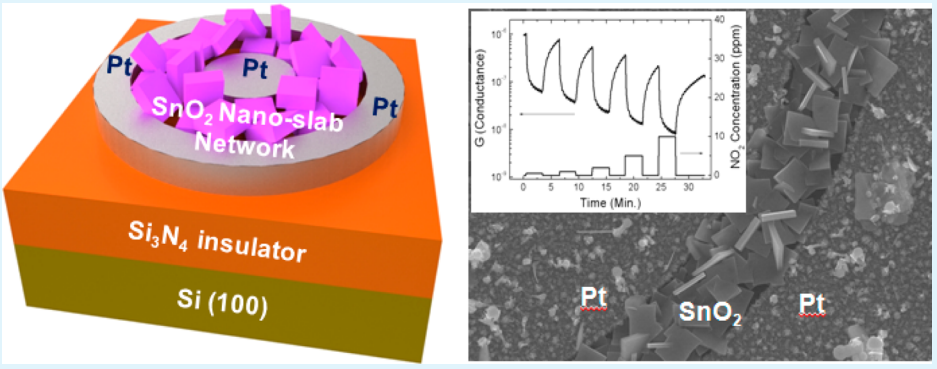

ABSTRACT: Among the various metal oxides, SnO_2 has been most widely exploited as a semiconductor gas sensor for its excellent functionalities. Models illustrating the sensing mechanism of SnO_2 have been proposed and tested to explain experimentally derived "power laws". The models, however, are often based on somewhat simplistic assumptions; for instance, the net charge transfer from an adsorbate to a sensor surface site is assumed to occur only by integer values independent of the crystallographic planes. In this work, we use layer-shaped SnO_2 crystallites with one nanodimension (1ND-crystallites) as NO_2 gas sensing elements under flat band conditions, and derive appropriate "power laws" by combining the dynamics of gas molecules on the sensor surface with a depletion theory of semiconductor. Our experimentally measured sensor response as a function of NO_2 concentration when compared with the theoretically derived power law indicates that sensing occurs primarily through the chemisorption of single NO_2 molecules at oxygen vacancy sites on the sensor surface.

KEYWORDS: *SnO_2 nanoslab, NO_2 sensor, gas sensing mechanism, flat band condition*

INTRODUCTION

Solid state n-type semiconductors, metal oxides in general and tin dioxide (SnO_2) in particular, have been widely exploited as gas sensors. Commercially available gas sensors, that normally operate in the range of temperatures between 100 and 400 °C, are made mainly of microcrystalline SnO_2 films and used for detection of gaseous species down to several parts per million (ppm) concentrations. As the needs for higher sensitivity gas sensors grow in the medicine, automotive, healthcare, and aerospace industries, there emerges a strong motivation to develop sensors which are capable of sensing gas concentration changes down to several parts per billion (ppb). The sensing mechanism relies on interactions between the dominating adsorbed molecular- or atomic-ionic species (adsorbates) and the semiconductor surface. Thus, the sensor sensitivity can be enhanced by securing a high surface-to-volume ratio of semiconducting materials. Recently, various types of nanocrystalline metal oxides with ultra high surface-to-volume ratio have been proposed as the ppb-level gas sensors.[1−20]

Received: October 6, 2013
Accepted: December 5, 2013
Published: December 5, 2013

ACS Publications © 2013 American Chemical Society

Depending on the number of dimensions which are nanostructured, nanocrystalline materials can be classified into three categories: layer-shaped crystallites with one nanodimension (1ND-crystallites), filamentary crystallites with two nanodimensions (2ND-crystallites), and equiaxed crystallites with three nanodimensions (3ND-crystallites). In the case of SnO_2, nanodiskettes/sheets/slabs[17−19] are 1ND-crystallites, nanowires/belts/ribbons[6−9] are 2ND-crystallites, and nanograins/spheres[3,4,20] are 3ND-crystallites. The 1ND-crystallites have more merits in gas sensing application than the 2ND- and 3ND-counterparts for several reasons. (See section S1 in the Supporting Information for a comparison of the SnO_2 gas sensing properties of 1ND-, 2ND-, and 3ND-crystallites.)

The gas sensing process can be divided into three successive steps: (i) the dynamic process of adsorption and/or reactions of gases on the sensor surface, (ii) the accumulation or depletion process of surface charges by the adsorbates, and (iii) the change of conductance of the sensing materials which is the indicator of the gas sensing.[21−26] It is known that the kind and density of adsorbates depend strongly on the surface temperature.[27,28]

The density of adsorbates depends also on the gas concentration, and it is empirically known that

$$S = K_{gas} \cdot C_{gas}^{\gamma} \quad (1)$$

where S is the sensor response generally defined as $G_0/G - 1$ (G_0 and G respectively denote the electrical conductance of a semiconductor gas sensor before and after exposure to the target gas) and C_{gas} is the concentration of the target gas. Here the power law exponent γ is specific to the kind of target gas for a given sensing material.[2,8,29,30] There were several attempts to derive the "power laws" by combining the dynamics of gases on the sensor surface with a depletion theory of semiconductor.[21−24,26,31]

Theoretical explanations are often based on assumptions that are too simplistic. For example, it has long been assumed that (i) the net charge transfer from an adsorbate to a sensor surface site occurs only by integer values and (ii) the amount of net charge transfer is fixed for a sensing material regardless of the types of the crystallographic planes. However, any standard quantum chemical calculation would indicate that charge transfer between an adsorbate molecule and the sensor surface involves a fraction of an electron charge, and the amount has a dependence on the local atomistic environment of the adsorption site, which depends on the exposed crystallographic plane, or defects like vacancies, dislocations, edges, and so forth. Some of these points have been illustrated by density functional theory (DFT) calculations of Maiti et al.[32]

The depletion theory of a semiconductor deals with the distribution of electrons between surface state and bulk. The distribution of electrons in a semiconductor can be calculated by using the Poisson equation. The solution of the Poisson equation requires the rectilinear (1D), cylindrical (2D), and spherical (3D) coordinate for 1ND-crystallites, 2ND-crystallites, and 3ND-crystallites, respectively. So far most of the theoretical works on nanosensors focused on 2ND-crystallites and 3ND-crystallites and ignored the angular dependence of the charge distribution in the nanostructures to obtain the analytical solutions.[26,27] However, it is necessary to take the angular dependence into consideration for a rigorous calculation, as both the reaction and the charge transfer depend on the kind of crystallographic facets.[32,33] In this regard, 1ND-crystallites are ideal to get an analytic solution of the Poisson equation, since the charge distribution in this structure has no angular dependence.

Under flat band conditions, most of the charges in the crystallites are free to move and are captured by adsorbed species. The amount of net charge transfer can be calculated if the information on the concentration of adsorbates, the amount of net charge transfer per an adsorbate, and the sort of the crystallographic planes is given. The concentration of adsorbates is proportional to the powers of gas concentration with a specific proportional constant to a specific crystallographic plane. Thus, the amount of captured charges will be approximately proportional to the powers of gas concentration if one crystallographic plane is dominantly larger than other planes as is the case of 1ND-crystallites. From the amount of the captured charge, we can calculate the conductance change and the "power law" can be easily derived.

Another important issue in the sensor research field is the identity of the sensor surface site which mainly contributes to the sensing mechanism. There exist spectra of opinions: Some insist that there is no reaction of the adsorbates with oxygen vacancies on the sensor surface at the sensor operation temperature range (100−400 °C),[8] while others suggest that reactions of the adsobates with the oxygen vacancies exist but this does not contribute to the main sensing mechanism because of the low density of the surface vacancies.[23,32] Another group of researchers even claims that the main sensing reaction occurs between the adsorbates and oxygen vacancies as a lot of surface oxygen vacancies *do* exist.[34,35] This controversy still remains unsettled. As the dynamics of chemical reaction between a specific adsorbate and an oxygen vacancy must be different from that between the adsorbate and a defect-free surface site, it is expected that the two cases lead to a different power law dependence. Thus, the main reaction site can be identified by analyzing the power law nature of sensor response with adequate assumptions.

In this article, we report a highly sensitive gas sensor based on self-assembled tin oxide nanoslabs (1ND-crystallites). By using the gas sensor, we detected NO_2 gas at various concentrations in order to obtain a relationship between the sensor response and the concentration of NO_2 gas under flat band conditions. The results were used to identify the main NO_2 sensing mechanism on the surface of SnO_2 nanoslabs.

EXPERIMENTAL PROCEDURES

Sample Preparation. Preparation of Metal Electrodes. 1.5 μm thick Si_3N_4 thin film was deposited by PECVD on a Si(001) wafer. Then, 100 nm thick Pt interdigitated electrodes (IDEs) were formed on the substrate by e-beam evaporation.

Synthesis of SnO Nanoslabs. *In situ* growth of SnO nanoslabs was carried out by thermal evaporation directly onto the substrate maintained at 500 °C in a horizontal two-zone tube furnace system. A horizontal quartz tube (inner diameter 20 mm, length 100 cm) was mounted inside the furnace, and the second heating zone is located 40 cm downstream from the center of the first heating zone. SnO powders (99.99% wt % purity) were loaded at the center of the first heating zone in an alumina boat. The Pt IDE-patterned Si_3N_4/Si(001) substrate on the quartz plate was loaded at the center of the second heating zone. At atmospheric pressure and the equilibrium of the Ar carrier gas flow at 1000 sccm, the quartz tube was heated for 180 min (the first zone at 1000 °C and the second zone at 500 °C) and kept for 30 min.

Transformation of SnO into SnO_2. Post-thermal annealing of the as-synthesized SnO nanoslabs was performed at 700 °C for 150 min in an Ar environment to obtain stable rutile structured SnO_2 nanoslabs.

Characterization of SnO_2 Nanoslabs. The general morphologies of SnO_2 nanoslabs were characterized using FE-SEM (JEOL JSM-6500F) measurements. The XRD (RIGAKU D/MAX-2500) data were

analyzed using a standard diffractometer with Cu Kα radiation in the θ–2θ configuration. The structural characterization was also carried out by TEM equipment (FE-TEM FEI TM G2 F30).

Analysis of Sensing Property. The NO_2 gas sensing properties were measured using a computer-controlled characterization system, which consisted of a computer, a chamber, a power source for heating, mass flow controllers, a digital multimeter (Agilent, Model No. 34411A), and an electrometer (Keithley, Model No. 6517A). The sensor was located on the hot chuck inside the chamber, and the temperature of the sensor was controlled by using hot chuck. The measurements of the conductance of the SnO_2 nanoslab gas sensor were accomplished at 300 °C under different concentrations of NO_2 exposures by using N_2 as a carrier gas. The flow rate was constantly maintained at 1000 standard cubic centimeter per minute (sccm) by using mass flow controllers.

RESULTS

Figure 1a shows a schematic diagram of a sensor device. The plan-view field-emission scanning electron microscopy (FE-SEM)

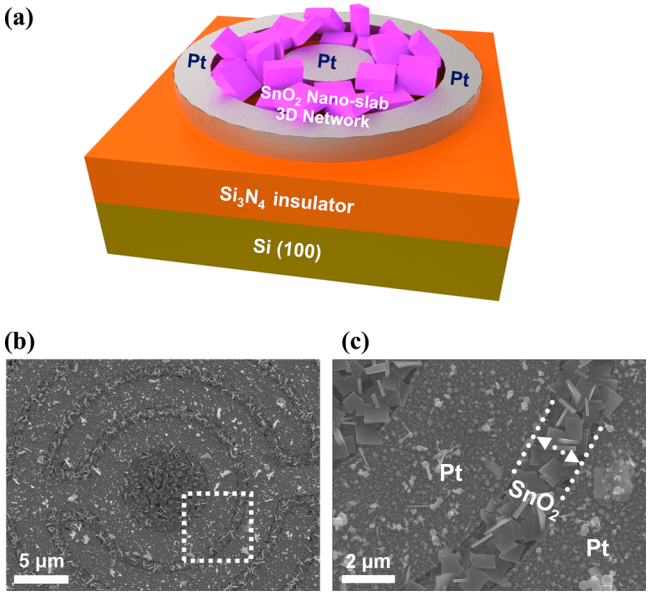

Figure 1. (a) The schematic diagram of the SnO_2 nanoslab 3D network sensor device. (b) Plan-view FE-SEM image of the SnO_2 nanoslab 3D networks synthesized on Pt IDE patterns. (c) Enlarged image of the area within the frame shown in part b.

images of SnO_2 nanoslab networks on the Pt IDE-patterned Si_3N_4/Si(001) substrate are shown in Figure 1b and c. These two images illustrate that the interconnected standing nanoslabs are packed only in the region between the Pt electrodes. From the images, the lateral, vertical, and thickness dimensions of a nanosheet can be estimated to be ~1 μm, ~1 μm, and ~100 nm, respectively.

The XRD pattern of a nanoslab (Figure 2a) was in clear correspondence with a rutile SnO_2 structure with space group $P4_2/mnm$, and lattice parameters $a = b = 4.734$ Å and $c = 3.185$ Å (JCPDS 21-1250). The high-resolution TEM (HR-TEM) image (Figure 2b) also reveals a single crystalline phase with a rutile structure having no planar dislocations. The corresponding fast Fourier transformation (FFT) pattern (Figure 2b, inset) further indicates that the SnO_2 nanoslab has the (101) face primarily exposed with preferred growth directions along [010] and $[10\bar{1}]$, respectively. (The information on the XRD and HR-TEM analysis of a tin oxide nanoslab before thermal annealing is presented in section S2 of the Supporting Information.)

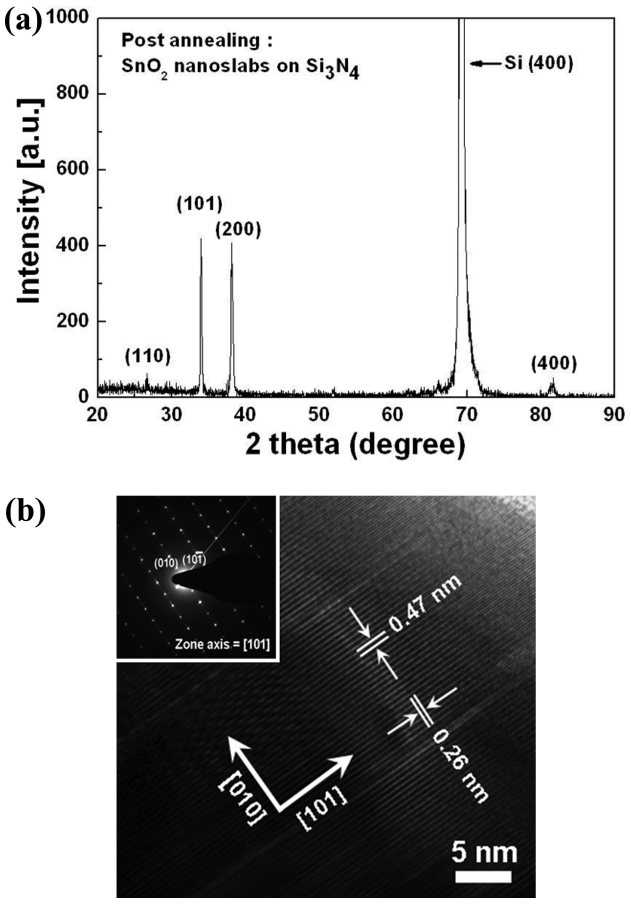

Figure 2. (a) XRD pattern of a thermally annealed nanoslab with a rutile SnO_2 structure. (b) HR-TEM image of the SnO_2 nanoslab. The inset shows a SAED pattern of the HR-TEM image.

In the following, we investigate the sensing response of the (101) surface with a specific analyte, i.e., NO_2, one of the most frequently studied oxidizing gases. In the literature, NO_2 detection experiments by SnO_2 sensors have mostly been performed in air.[6,7,14,24,26,33] In such a case, the NO_2 is in competition with oxygen (O_2) in adsorbing onto the surface of SnO_2, which complicates the analysis of the oxidation kinetics. To eliminate O_2 influences in our study, we evacuated air in the test chamber first, then injected the test gas mixed only with nitrogen (N_2) to achieve the desired concentration, and then maintained the flow rate at 1000 standard cubic centimeter per minute (sccm). If the Pt/SnO_2 contact is not Ohmic, the introduction of NO_2 not only influences the SnO_2 surface potential but also influences the Shottky barrier potential height in the contact. In order to eliminate the influences from the Pt/SnO_2 metal/semiconductor contact, we performed the NO_2 sensing experiments at 300 °C.[35] Results of the conductance change of the nanoslab sensor upon cyclical exposure to NO_2 at different concentrations are shown in Figure 3. A noticeable drop in conductance is discernible even at NO_2 levels as low as 500 ppb, with significant drops at higher concentrations. Figure 4 shows a low resolution cross-TEM image of a SnO_2 nanoslab network. As shown in the image, the SnO_2 nanoslabs synthesized in our experiments were mostly standing rather than lying. In an all-standing configuration, the NO_2 binding occurs mostly on both sides of the nanoslabs. Given that the length L and height H of the nanoslab (~1 μm) are much larger than the depth D (~100 nm), each nanoslab can be approximated as a

dx.doi.org/10.1021/am404397f | ACS Appl. Mater. Interfaces 2014, 6, 357–363

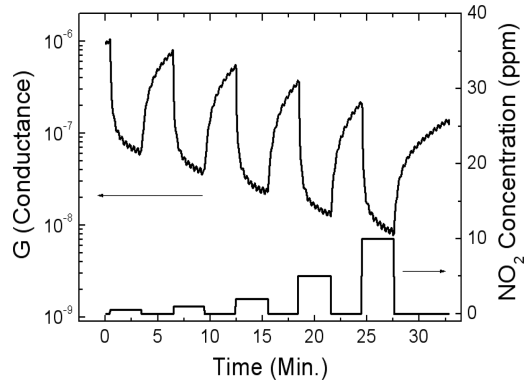

Figure 3. The conductance dependence of a SnO_2 nanoslab network sensor upon cyclic exposure to NO_2 gas with different concentrations at 300 °C.

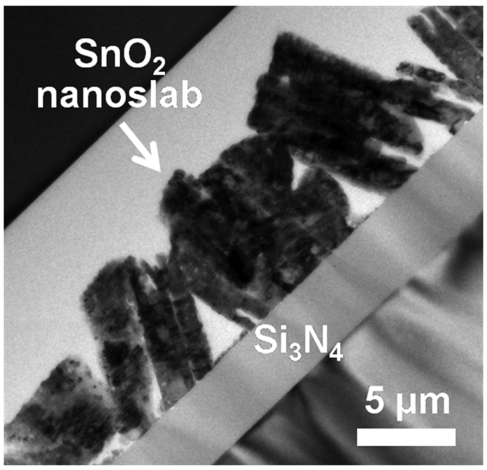

Figure 4. The low resolution cross-TEM image of the SnO_2 nanoslab network prepared by FIB.

1ND-crystallite. Solving the 1D Poisson equation with appropriate boundary conditions yields the relation $\Delta E/k_B \sim [D/(8)^{1/2}\lambda_D]^2$, where ΔE is the potential energy difference between the center and surface of the nanoslab and λ_D is the Debye length. (See section S3 in the Supporting Information for the 1D Poission equation for a SnO_2 nanoslab.) When ΔE is comparable with the thermal energy, it leads to a homogeneous electron concentration in the nanoslab, which in turn results in the flat band case.[20] This happens for $\lambda_D \geq D/(8)^{1/2} \sim 35$ nm. Such Debye lengths are indeed attained at our experimental temperatures of $T \sim 300$ °C. In the inert gas (N_2) environment, the nanoslab behaves like a quasi-conductive element, while upon exposure to NO_2 almost all the electrons in the nanoslab are free to move to be captured by surface acceptors, leading to significant conductance drops. The schematic diagram explaining the operation of the SnO_2 nanoslab network NO_2 sensor is shown in Figure 5a.

Figure 5b shows the relationship between the NO_2 concentration and the sensor response. The sensitivity of the SnO_2 nanoslab network sensor is more than 1000% for 500 ppb NO_2 concentration. This indicates that even for sub-ppm concentrations of NO_2 gas the nanonetwork behaves like a conductance switch. By fitting our data to the power law model (eq 1), we obtain the power law exponent $\gamma \approx 0.69$.

Derivation of Power Laws. The power law dependence of the sensor response on adsorbate concentration depends on the

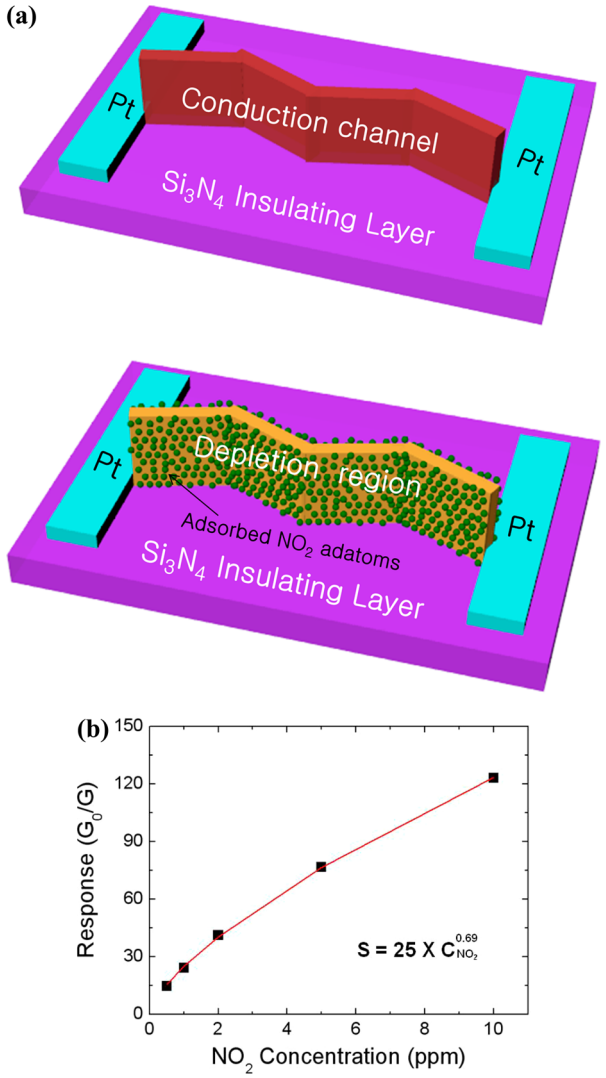

Figure 5. (a) Schematic diagram explaining the chemical gating of the standing SnO_2 nanoslab network sensor. Before the exposure to NO_2 gas, the nanoslab network acts as a conducting channel (upper). After the exposure to NO_2 gas, the network turns into a fully depleted region of carriers due to the influence from the adsorbed NO_x adatom structures (lower). (b) The relationship between the response of a SnO_2 nanoslab network sensor and NO_2 concentration at 300 °C.

order of the adsorption reaction, more specifically whether it involves one or more NO_2 molecules. Maiti et al.[32] have explored two different situations: (1) in which single NO_2 moecules adsorb in various configurations and (2) in which two NO_2 molecules react to form stable NO_3 adsorbates (with a weakly bounded NO desorbing subsequently). In their analysis on a SnO_2 nanoribbon, two different surfaces were considered. Here we consider binding only to the predominantly exposed surface (101) in our 1ND sensors. Table 1 summarizes the computed binding energy and charge transfer from ref 32 for important adatom structures resulting from NO_2 and NO_3 to the $(10\bar{1})$ surface of SnO_2 (note that $(10\bar{1})$ and (101) are chemically equivalent surfaces for a rutile SnO_2 structure). The charge transfer amounts are based on partial charge calculation on each atom according to the Mulliken population analysis.[37]

Given that the NO_3 adatom structures possess higher binding energy and involve larger charge transfer, we first discuss a theoretical model to relate the power law exponent α to

dx.doi.org/10.1021/am404397f | ACS Appl. Mater. Interfaces 2014, 6, 357−363

Table 1. Summary of the Computed Binding Energy and Charge Transfer for Important NO_x Adatom Structures Resulting from NO_2 Gas to the $(10\bar{1})$ Surface of SnO_2[a]

adsorbed site	adatom structure	binding energy (kcal/mol)	net charge transfer (el.)
defect free surface	$(NO_3)_1$	14.3	−0.30
	$(NO_3)_2$	25.5	−0.41
	$(NO_2)_1$	11.2	−0.17
	$(NO_2)_2$	13.8	−0.17
bridging oxygen vacancy	$(NO_2)_{2,VAC}$	41.4	−0.51

[a]Structure names follow the convention $(\,)_1$, one single bond to a surface Sn; $(\,)_2$, two single bonds, each to a different (and neighboring) Sn atom; $(\,)_{2,VAC}$, one bond to Sn and bridging O atom to an oxygen vacancy. After Maiti et al.[32]

electronic charge transfer from the SnO_2 surface to an NO_3 adatom structure. Equation 2 describes the formation of an NO_3 adatom on the defect-free surface, in a process that involves two NO_2 molecules:

$$NO_2^{gas} + \alpha_1 \cdot e^- + S_A \leftrightarrow NO_{2,S_A}^{-\alpha_1}$$

$$NO_2^{gas} + \alpha_2 \cdot e^- NO_{2,S_A}^{-\alpha_1} \leftrightarrow NO_{3,S_A}^{-(\alpha_1+\alpha_2)} + NO^{gas} \quad (2)$$

where NO_2^{gas} and NO^{gas} are NO_2 and NO molecules in a gaseous state in the chamber, α_1 and α_2 are charge transfer numbers, e^- is an electron, S_A is an adsorption site of the nanosheet surface, and $NO_{2,S_A}^{-\alpha_1}$ and $NO_{3,S_A}^{-(\alpha_1+\alpha_2)}$ are NO_2 and NO_3 adatom structures, respectively.

By using the mass action law,

$$k_{ads} \cdot [S_A] \cdot n_s^{\alpha} \cdot {P_{NO_2}}^2 = k_{des} \cdot [NO_{3,S_A}^{-\alpha}] \cdot P_{NO} \quad (3)$$

where k_{ads} and k_{des} are reaction constants, n_s is the electron density at the surface (and is a function of the surface concentration of adsorbates), P_{NO_2} is the gas pressure in the chamber, [...] denotes surface density, and $\alpha = \alpha_1 + \alpha_2$. Note that, under the flat band condition, n_s is the homogeneous concentration of electrons throughout the whole SnO_2 nanoslab. The surface coverage with chemisorbed NO_3 species is defined as $\theta = [NO_{3,S_A}^{-\alpha}]/[S_{A,t}]$, where $[S_{A,t}]$ is the total concentration of the available adsorption site, occupied or unoccupied. By using the conservation of surface sites, $[S_A] + [NO_{3,S_A}^{-\alpha}] = [S_{A,t}]$, eq 3 can be rewritten as

$$k_{ads} \cdot (1 - \theta) \cdot n_s^{\alpha} \cdot {P_{NO_2}}^2 = k_{des} \cdot \theta \cdot P_{NO} \quad (4)$$

If n_b is the electron density for the pristine material (i.e., $\theta = 0$), the condition of electrical neutrality yields the relation $\alpha \cdot \theta \cdot [S_{A,t}] \cdot$ area + $n_s \cdot$volume = $n_b \cdot$volume, where "area" and "volume" relate to the total exposed (101) surface area and the total volume of the nanoslab, respectively. In terms of surface adsorbate coverage (θ), the charge neutrality condition can be rewritten as

$$\theta = \frac{(n_b \cdot \text{volume}) \cdot (1 - n_s/n_b)}{\alpha \cdot [S_{A,t}] \cdot \text{area}} \quad (5)$$

Figure 3 shows that the number of carrier electrons in the nanoslab tends to be depleted down to 1% of the original number as the concentration of NO_2 gas molecules increases. If the adsorption of the NO_3 species is the main kinetics involved in the depletion of the carrier electrons, this implies that the total number of electrons in the nanoslab ($n_b \cdot$volume) is almost equal to the maximum number of electrons which can be captured by the adsorbed NO_3 species ($\alpha \cdot [S_{A,t}] \cdot$area) and the above equation can be approximated as

$$\theta \approx 1 - n_s/n_b \quad (6)$$

Inserting eq 6 into eq 4 and using the relation $n_b \gg n_s$, we obtain

$$n_s \approx \{(k_{des} \cdot n_b \cdot P_{NO})/k_{ads}\}^{1/(1+\alpha)} \cdot P_{NO_2}^{-[2/(1+\alpha)]} \quad (7)$$

As for the NO_3 adatom mechanism, P_{NO} is proportional to θ (and independent of P_{NO_2}) and therefore essentially a constant when $G_0/G \gg 1$. This is because the number of NO molecules formed is exactly equal to the number of NO_3 adatoms formed on the surface.

The conductance G is proportional to n_s under flat band conditions, and the gas response S is proportional to the inverse of G. Thus, the sensor response S is proportional to $P_{NO_2}^{2/(1+\alpha)}$. As the partial pressure of NO_2 gas is proportional to the concentration of it, the relation between sensor response S and NO_2 gas concentration C_{NO_2}, then, can be described as

$$S = K_{NO_2} \cdot C_{NO_2}^{2/(1+\alpha)} \quad (8)$$

Comparing eq 8 with eq 1, we have

$$\gamma = \frac{2}{1 + \alpha} \quad (9)$$

Now, let us consider the situation in which the sensor response is dominated by the adsorption of single NO_2 molecules at available surface sites S_A of the (101) surface.

If the adatom withdraws β electrons from the surface, such a process can be described as

$$NO_2^{gas} + \beta \cdot e^- + S_A \leftrightarrow NO_{2,S_A}^{-\beta} \quad (10)$$

where NO_{2,S_A} represents a surface-adsorbed NO_2. By using the mass action law,

$$k_{ads} \cdot [S_A] \cdot n_s^{\beta} \cdot P_{NO_2} = k_{des} \cdot [NO_{2,S_A}^{-\beta}] \quad (11)$$

Now the surface coverage with chemisorbed NO_2 species is defined as $\theta = [NO_{2,S_A}^{-\beta}]/[S_{A,t}]$, and from the relation $[S_A] + [NO_{2,S_A}^{-\beta}] = [S_{A,t}]$, eq 11 can be rewritten as

$$k_{ads} \cdot (1 - \theta) \cdot n_s^{\beta} \cdot P_{NO_2} = k_{des} \cdot \theta \quad (12)$$

Our assumption that the adsorption of the NO_2 species is the main kinetics involved in the depletion of the carrier electrons leads to the relation $\theta \approx 1 - n_s/n_b$, and by inserting this into eq 12 and using the relation $n_b \gg n_s$, we obtain

$$n_s \approx \{(k_{des} \cdot n_b)/k_{ads}\}^{1/(1+\beta)} \cdot P_{NO_2}^{-[1/(1+\beta)]} \quad (13)$$

The sensor response then can be written as

$$S = K_{NO_2} \cdot C_{NO_2}^{1/(1+\beta)} \quad (14)$$

Comparing eq 14 with eq 1, we have

$$\gamma = \frac{1}{1 + \beta} \quad (15)$$

dx.doi.org/10.1021/am404397f | ACS Appl. Mater. Interfaces 2014, 6, 357−363

DISCUSSIONS

Equations 9 and 15 derived in the previous section are the important power laws that can be compared with our experimental value of γ to gain insight into the molecular mechanism of NO_2 sensing by our 1ND SnO_2 nanoslabs. Here are our observations:

(1) Given that charge transfer $\alpha < 1$, the experimental value of $\gamma \sim 0.69$ cannot be explained by eq 9. It is more consistent with eq 15. This clearly means that, in our case, sensing is dominated by the adsorption of single NO_2 molecules, rather than the formation of NO_3 species as found on the nanoribbon surface.[32]

(2) Physically, the above makes sense because on our SnO_2 nanoslabs the probability of two NO_2 molecules meeting is much smaller than on a 2ND system like a nanoribbon. This is especially true at the sub-ppm gas concentration levels used in this work.

(3) The theoretical value of net charge transfer from a defect free surface site to a NO_2 molecule is $\beta = 0.17$ el., as shown in Table 1. By inserting this value into eq 15, we obtain $\gamma = 0.85$, which is considerably larger than the experimentally obtained value $\gamma = 0.69$. With the theoretical value of net charge transfer from a bridging O vacancy site to a NO_2 molecule ($\beta = 0.51$ el.), γ is calculated as 0.66, which is very close to 0.69. Various types of vacancies exist in SnO_2. Among them, subsurface vacancies are expected to contribute little in net charge transfer. Judging from the high resolution TEM image of the SnO_2 nanoslab (Figure 2b), O vacancies arising from the kinks, steps, or dislocations are also ruled out. Possibly different kinds of O vacancies may arise from the slab−slab interfaces. However, they can be ignored, as the numbers of the vacancies would be much less than the bridging O vacancies in *perfect* nanoslabs.

(4) One must be careful in using DFT-computed charge transfer values because the numbers are not unambiguous but depend on computational details (e.g., basis set, exchange-correlation functional, charge partitioning method, etc.).[37] In addition, one needs to identify the amount of charge transfer due to the capture of conduction electrons as discussed here versus that due to reorganization of valence electrons due to local chemical rebonding, which mandates further analysis.

(5) Even though limits and uncertainties exist in DFT as mentioned in point 4 above, the fact that the bridging O vacancies contribute mainly to the NO_2 sensing receives further support from the recovery behavior of the sensor, which is illustrated in Figure 3. The figure clearly shows the sensor hardly recovers its original conductance after repeated adsorption−desorption cycling. This result confirms that indeed the sensing mechanism in our case is dominated by the adsorption of single NO_2 molecules at surface O vacancies. In such a case, one of the O atoms of NO_2 fills the vacancy, and the weakly bonded NO desorbs from the surface, as was also originally suggested by Maiti et al.[32]

It is also important to discuss the number density of surface oxygen vacancies of SnO_2 nanoslabs. Let us assume that the oxygen vacancies are distributed uniformly in the nanoslabs and break a SnO_2 sheet into "layers" parallel to (101). Suppose the thickness d of each repeating layer is ~0.5 nm. If $[V_{O,bulk}]$ is the concentration of oxygen vacancies in the slab, then the surface concentration of the oxygen vacancies is $[V_{O,t}] \sim d/D \cdot [V_{O,bulk}]$, where D is the slab thickness of ~100 nm. When oxygen vacancies are the main sensing reaction sites, $[V_{O,t}] = [S_{A,t}]$. Thus, the total concentration of the available adsorption site $[S_{A,t}]$ is ~0.5% of the total concentration of oxygen vacancies in the slab. This dilemma may be solved by the observations and estimations that oxygen vacancies are not distributed uniformly inside SnO_2 nanomaterials but located mainly on the surface regardless of the method of synthesis.[34,35,38−41]

CONCLUSIONS

We report a highly sensitive SnO_2 nanoslab NO_2 gas sensor by employing a simple and cost-effective thermal deposition process for the first time. From observations of orders-of-magnitude conductance drops and theoretical calculations, it was confirmed that the sensor acts as a conductance switch in which a flat band condition is reached at 300 °C through double chemical gating of standing SnO_2 nanoslabs by NO_2. The observed relationship between the sensor response and the NO_2 gas concentration was explained by assuming chemisorption of NO_2 molecules at a large number of bridging O vacancy sites on the predominantly exposed (101) surface of the SnO_2 nanoslabs.

ASSOCIATED CONTENT

Supporting Information

Section S1: Comparison of SnO_2 gas sensing properties of 1ND-, 2ND-, and 3ND-crystallites. Section S2: XRD and HR-TEM analysis of tin oxide nanoslab before thermal annealing. Section S3: 1D Poission equation for a SnO_2 nanoslab. This material is available free of charge via the Internet at http://pubs.acs.org.

AUTHOR INFORMATION

Corresponding Authors

*E-mail: sunglyulm@gmail.com (S.M.).
*E-mail: kimsw1@skku.edu (S.-W.K.).
*E-mail: maiti2@llnl.gov (A.M.).

Notes

The authors declare no competing financial interest.

ACKNOWLEDGMENTS

This work was supported by the Program of Regional Innovation Center (Woosuk University) which was conducted by the Ministry of Trade, Industry and Energy of the Korean Government. This work was also supported by the Basic Research Program (2009-0083540) of the National Research Foundation of Korea (NRF) grant funded by the Ministry of Science, ICT & Future Planning (MSIP). The work by one of the authors (A.M.) was performed under the auspices of the U.S. Department of Energy by Lawrence Livermore National Laboratory under Contract DE-AC52-07NA27344.

REFERENCES

(1) Corcoran, P.; Shurmer, H. V.; Gardner, J. W. *Sens. Actuators, B* **1993**, *15*, 32−37.
(2) Barsan, N.; Schweizer-Berberich, M.; Gopel, W. *Fresenius' J. Anal. Chem.* **1999**, *365*, 287−304.
(3) Lu, F.; Liu, Y.; Dong, M.; Wang, X. *Sens. Actuators, B* **2000**, *66*, 225−227.
(4) Liu, Y.; Koep, E.; Liu, M. *Chem. Mater.* **2005**, *17*, 3997−4000.
(5) Epifani, M.; Diaz, R.; Arbiol, J.; Comini, E.; Sergent, N.; Pagnier, T.; Siciliano, P.; Faglia, G.; Morante, J. R. *Adv. Funct. Mater.* **2006**, *16*, 1488−1498.

(6) Comini, E.; Faglia, G.; Sberveglieri, G.; Pan, Z.; Wang, Z. L. *Appl. Phys. Lett.* **2002**, *81*, 1869−1871.
(7) Law, M.; Kind, H.; Messer, B.; Kim, F.; Yang, P. *Angew. Chem., Int. Ed.* **2002**, *41*, 2405−2408.
(8) Kolmakov, A.; Zhang, Y.; Cheng, G.; Moskovits, M. *Adv. Mater.* **2003**, *15*, 997−1000.
(9) Wang, Y.; Jiang, X.; Xia, Y. *J. Am. Chem. Soc.* **2003**, *125*, 16176−16177.
(10) Zhang, D.; Liu, Z.; Li, C.; Tang, T.; Liu, X.; Han, S.; Lei, B.; Zhou, C. *Nano Lett.* **2004**, *4*, 1919−1924.
(11) Wan, Q.; Li, Q. H.; Chen, Y. J.; Wang, T. H.; He, X. L.; Li, J. P.; Lin, C. L. *Appl. Phys. Lett.* **2004**, *84*, 3654−3656.
(12) Liu, Y.; Liu, M. *Adv. Funct. Mater.* **2005**, *15*, 57−62.
(13) Wang, B.; Zhu, L. F.; Yang, Y. H.; Xu, N. S.; Yang, G. W. *J. Phys. Chem. C* **2008**, *112*, 6643−6647.
(14) Choi, Y.-J.; Hwang, I.-S.; Park, J.-G.; Choi, K. J.; Park, J.-H.; Lee, J.-H. *Nanotechnology* **2008**, *19*, 095508.
(15) Huang, J.; Wan, Q. *Sensors* **2009**, *9*, 9903−9924.
(16) Moon, S. E.; Lee, H.-Y.; Park, J.; Lee, J.-W.; Choi, N.-J.; Park, S.-J.; Kwak, J.-H.; Park, K.-H.; Kim, J.; Cho, G.-H.; Lee, T.-H.; Maeng, S.; Udrea, F.; Milne, W. I. *J. Nanosci. Nanotechnol.* **2010**, *10*, 3189−3192.
(17) Moon, C. S.; Kim, H.-R.; Auchterlonie, G.; Drennan, J.; Lee, J.-H. *Sens. Actuators, B* **2008**, *131*, 556−564.
(18) Dai, Z. R.; Pan, Z. W.; Wang, Z. L. *J. Am. Chem. Soc.* **2002**, *124*, 8673−8680.
(19) Kumar, B.; Lee, D.-H.; Kim, S.-H.; Yang, B.; Maeng, S.; Kim, S.-W. *J. Phys. Chem. C* **2010**, *114*, 11050−11055.
(20) Pang, G.; Chen, S.; Koltypin, Y.; Zaban, A.; Feng, S.; Gedanken, A. *Nano Lett.* **2001**, *1*, 723−726.
(21) Morrison, S. R. *The Chemical Physics of surfaces*; Plenum: New York, 1997; p 29.
(22) Barsan, N. *Sens. Actuators, B* **1994**, *17*, 241−246.
(23) Gergintschew, Z.; Förster, H.; Kositza, J.; Schipanski, D. *Sens. Actuators, B* **1995**, *26−27*, 170−173.
(24) Rantala, Tu.; Lantto, V.; Rantala, Ta. *Sens. Actuators, B* **1998**, *47*, 59−64.
(25) Ruhland, B.; Becker, Th.; Müller, G. *Sens. Actuators, B* **1998**, *50*, 85−94.
(26) Barsan, N.; Weimar, U. *J. Electroceram.* **2001**, *7*, 143−167.
(27) Comini, E.; Guidi, V.; Malagu, C.; Martinelli, G.; Pan, Z.; Sberveglieri, G.; Wang, Z. L. *J. Phys. Chem. B* **2004**, *108*, 1882−1887.
(28) Nitta, M.; Ostani, S.; Haradome, M. *J. Electron. Mater.* **1980**, *9*, 727−743.
(29) Akiyama, M.; Tamaki, J.; Miura, N.; Yamazoe, N. *Chem. Lett.* **1991**, *9*, 1611.
(30) Gardner, J. W.; Bartlett, P. N. *Sens. Actuators, B* **1994**, *18−19*, 211−220.
(31) Yamazoe, N.; Shimanoe, K. *Sens. Actuators, B* **2008**, *128*, 566−573.
(32) Maiti, A.; Rodriguez, J. A.; Law, M.; Kung, P.; McKinney, J. R.; Yang, P. *Nano Lett.* **2003**, *3*, 1025−1028.
(33) Batzill, M. *Sensors* **2006**, *6*, 1345−1366.
(34) Epifani, M.; Prades, J. D.; Comini, E.; Pellicer, E.; Avella, M.; Siciliano, P.; Faglia, G.; Cirera, A.; Scotti, R.; Morazzoni, F.; Morante, J. R. *J. Phys. Chem. C* **2008**, *112*, 19540−19546.
(35) Pan, J.; Ganesan, R.; Shen, H.; Mathur, S. *J. Phys. Chem. C* **2010**, *114*, 8245−8250.
(36) Hernández-Ramírez, F.; Tarancón, A.; Casals, O.; Arbiol, J.; Romano-Rodríguez, A.; Morante, J. R. *Sens. Actuators, B* **2007**, *121*, 3−17.
(37) Szabo, A.; Ostlund, N. S. *Modern Quantum Chemistry*, 1st ed. revised (paperback); Dover Publications: New York, 1996; p 151.
(38) Jarebski, Z. M.; Marton, J. P. *J. Electrochem. Soc.* **1976**, *123*, 299C−310C.
(39) Liu, Y.; Zhu, W.; Tan, O. K.; Yao, X.; Shen. *J. Mater. Sci.: Mater. Electron.* **1996**, *7*, 279−282.
(40) Varela, J. A.; Perazolli, L. A.; Cerri, J. A.; Leite, E. R.; Longo, E. *Ceramica* **2001**, *47*, 117.
(41) Xiong, H.-M.; Zhao, K. K.; Zhao, X.; Wang, Y.-W.; Chen, J. S. *Solid State Ionics* **2003**, *159*, 89−95.

NOTE ADDED AFTER ASAP PUBLICATION

This paper was published on the Web on December 16, 2013. Additional minor text corrections were included, along with replacing Figure 4, and the corrected version was reposted on December 18, 2013.